Chapter 4

Structure, Microstructure and Local Structure of $Co_xMn_{3-x}O_4$ (x = 1.00 to 2.00) Nanoparticles

4.1 Introduction

In this chapter, we investigate the evolution of structure in $Co_xMn_{3-x}O_4$, when x varies from 1.00 to 2.00. In section 4.2, we have undertaken the X-ray diffraction pattern to illustrate the structure which demonstrates the coexistence of dominating tetragonal phase (space group: $I41/amd$) with small fraction of cubic phase (space group: $Fd\bar{3}m$) for x = 1.00. With increase in x, cubic phase fraction is found to be increased and become dominating for x = 1.50, and with further increase in x, pure cubic phase (space group: $Fd\bar{3}m$) is observed for x = 1.75 and above. The structural phase transition is further investigated through the XANES and EXAFS analysis, which confirms that Mn^{3+} and Co^{3+} cations increase in octahedral site for both the phases with increase in x. For pure cubic phase samples, presence of Mn^{4+} in octahedral site is observed. Microstructural analysis shows the decrement in average particle size from 95 to 48 nm with increase in x from 1.00 to 2.00. The results of this chapter are summarized in section 4.3.

4.2 Structure and microstructure

4.2.1 Structural phase through X-ray diffraction

XRD patterns of $Co_xMn_{3-x}O_4$ (x = 1.0, 1.25, 1.50, 1.75 and 2.0) shown in **Figure 4.1**, match well with tetragonal and cubic phases corresponding to JCPDS card no. 77-0471 and 23–1237, respectively. We have demonstrated the evolution of (2 2 0) with x. (2 2 0) corresponding to the cubic phase when x = 2.00, gradually splits into two peaks as (2 2 0) and (2 0 0) which denotes the presence of a tetragonal phase with a decrease in x. It may be noted that the intensity of T(2 0 0) increases at the expense of C(2 2 0) with

decrease x from 2.00 to 1.00 **(Figure 4.1(a))**. The structural analysis has been carried out through Rietveld refinement using the space group $I41/amd$ and $Fd\bar{3}m$ for the samples having coexistence of cubic and tetragonal phases (x = 1.00, 1.25, 1.50) and using $Fd\bar{3}m$ for pure cubic phase (x = 1.75, 2.00) as depicted in **Figure 4.1(b)**. Refinement parameters are depicted in **Table 4.1**.

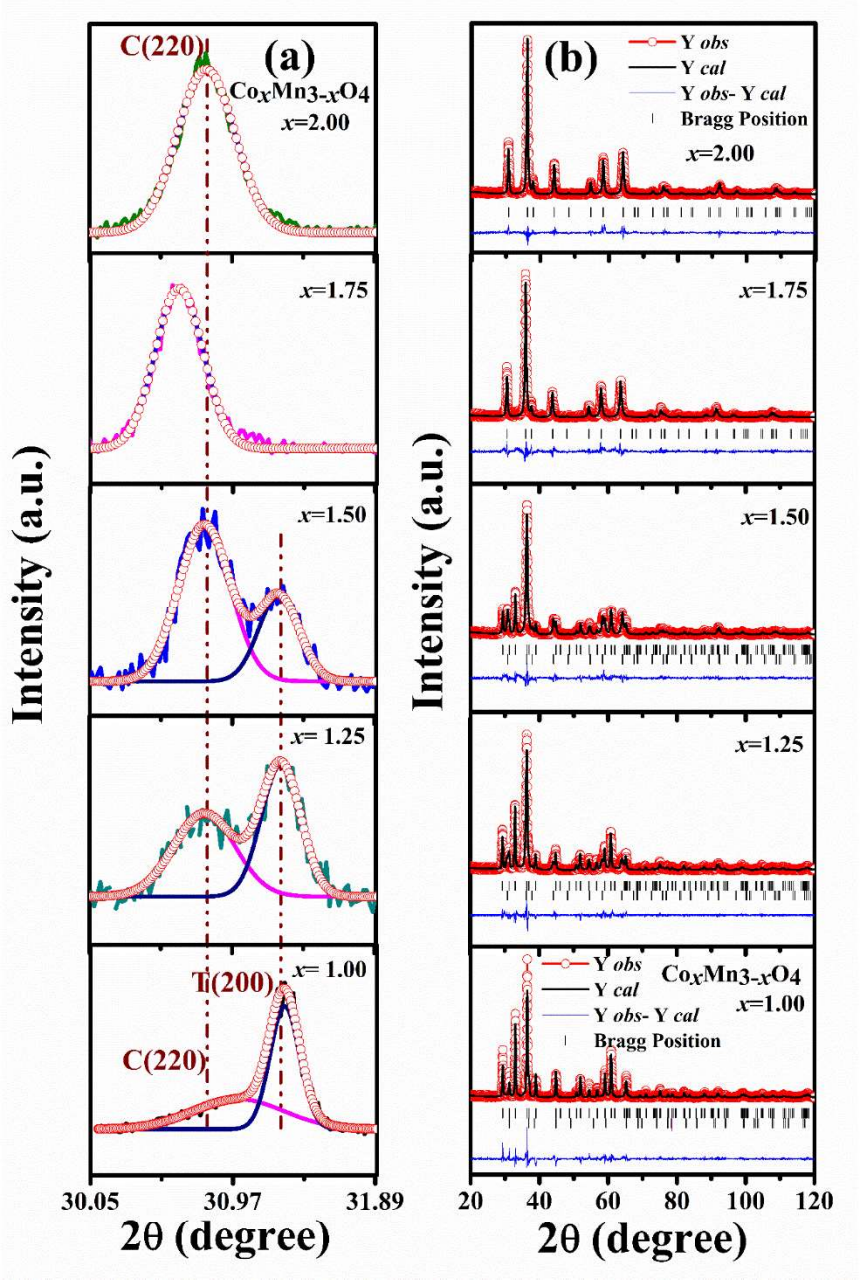

Figure 4.1: (a) Variation in XRD peak with x and (b) XRD pattern with Rietveld refinement of $Co_xMn_{3-x}O_4$ (x = 1.00, 1.25, 1.50, 1.75 and 2.00) nanoparticles.

For the best fitting, χ^2 is found to be minimum and lies between 1 to 2 for all the compositions. It is evident from **Table 4.1** that with decrease in *x*, pure cubic phase converts into dominating tetragonal phase for *x* = 1.00. The cell volume for the tetragonal phase is the same (~302.037 $Å^3$) irrespective of the samples, while for the cubic phase, it varies from 549.071 to 564.770 $Å^3$. It is noticed that the cell volume is found to be decreased irrespective of the phase as compared to the bulk mentioned in the International Centre for Diffraction Data (ICDD). From the fitting, it is observed that for *x* =1.00, where tetragonal phase is dominated Co mainly occupies A site and Mn mainly occupies the B site. When *x* = 2.00 having cubic symmetry, both Co and Mn are distributed in A and B sites. In intermediate compositions, when tetragonality reduces, the distribution of Co and Mn in A and B sites get reversed for both the phases. Further, crystallite size is determined using Williamson–Hall method from Bragg peak broadening using equation (4.1):

$$\beta cos\theta = k\lambda / D + 4\varepsilon sin\theta \qquad (4.1)$$

where k (~0.9), β, θ, D and ε represent the shape parameter, full width at half maximum (FWHM), Bragg angle, crystallite size and lattice strain, respectively [153]. From the slope of the plot β cosθ versus 4sinθ, the crystallite size is found to be 42, 30, 24, 28 and 28 nm for *x* = 1.00, 1.25, 1.50, 1.75 and 2.00, respectively **(Figure 4.2)**.

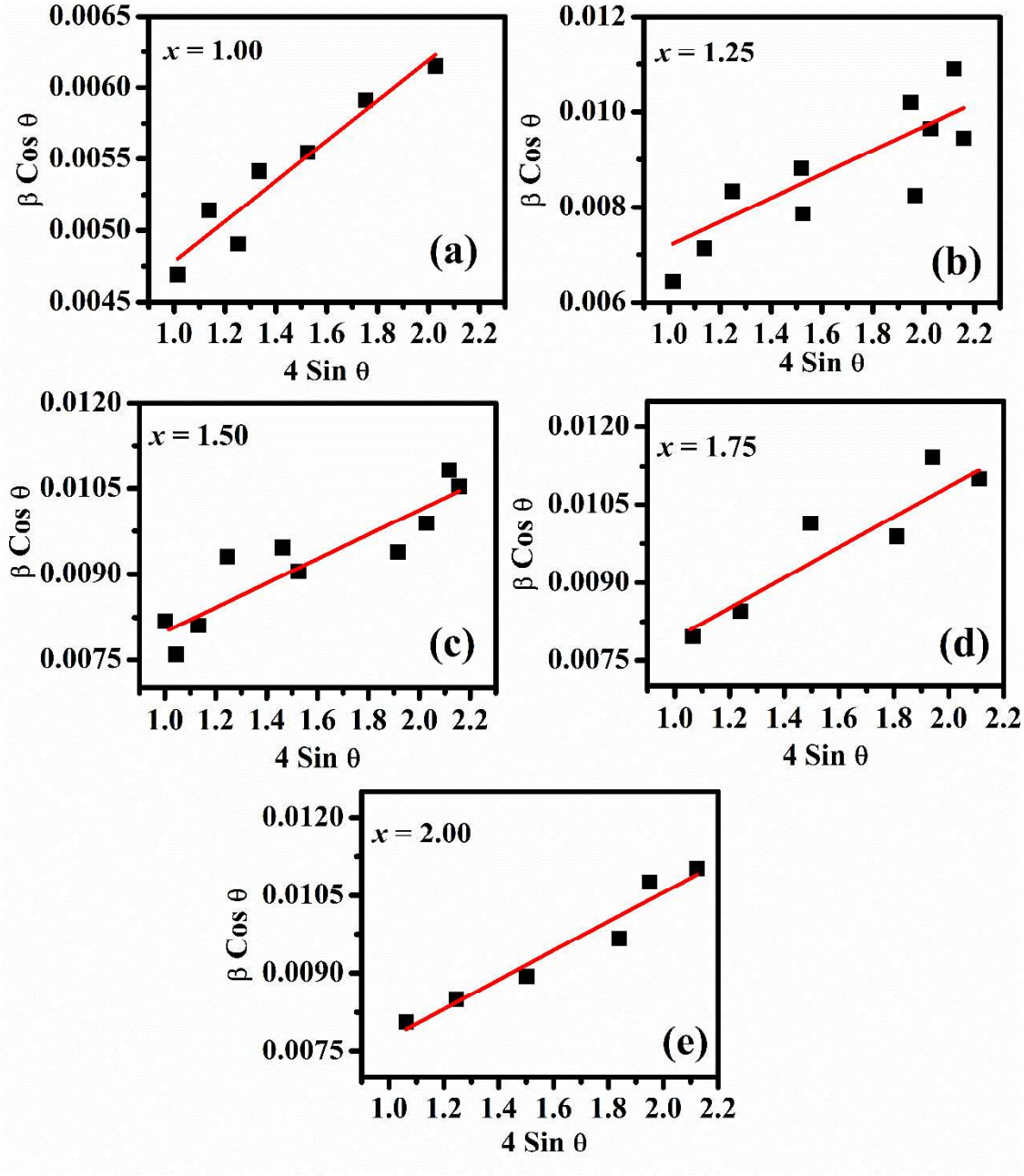

Figure 4.2: (a-e) Williamson-Hall (W-H) plots for x = 1.00 to 2.00.

Table 4.1: Structural parameters of $Co_xMn_{3-x}O_4$ nanoparticles at room temperature revealed from the Rietveld refinement.

	Composition having co-existence of tetragonal and cubic phase						**Pure Cubic**	
	Tetragonal			**Cubic**			**Cubic**	
Composition $Co_xMn_{3-x}O_4$	***x* = 1.00**	***x* = 1.25**	***x* = 1.50**	***x* = 1.00**	***x* = 1.25**	***x* = 1.50**	***x* = 1.75**	***x* = 2.00**
Space group	*I41/amd*	*I41/amd*	*I41/amd*	$Fd\bar{3}m$	$Fd\bar{3}m$	$Fd\bar{3}m$	$Fd\bar{3}m$	$Fd\bar{3}m$
Phase fraction	91.8(0.6)	67(1)	46.7(0.8)	8.2(0.7)	33.5(0.9)	53 (1)	100	100
a [Å]	5.7163 (1)	5.7230(3)	5.720(1)	8.189 (2)	8.2234(8)	8.2107(4)	8.2656(3)	8.2207(4)
b [Å]	5.7163 (1)	5.7230(3)	5.720(1)	8.189 (2)	8.2234(8)	8.2107(4)	8.2656(3)	8.2207(4)
c [Å]	9.2435 (4)	9.2497(6)	9.234(1)	8.189 (2)	8.2234(8)	8.2107(4)	8.2656(3)	8.2207(4)
Vol [$Å^3$]	302.0372	302.9529	302.0769	549.0717	556.1017	553.5292	564.770	555.542
Co/Mn (A site)	4b (0, 1/4, 3/8)	4b (0, 1/4, 3/8)	4b (0, 1/4, 3/8)	8a (1/8, 1/8, 1/8)	8a (1/8, 1/8, 1/8)	8a (1/8, 1/8, 1/8)	8a (1/8, 1/8, 1/8)	8a (1/8, 1/8, 1/8)
OccA/Co [%]	94	75	62	4	28	50	45	75
OccA/Mn [%]	6	25	38	96	72	50	55	25
Co/Mn [B site]	8c (0, 0, 0)	8c (0, 0, 0)	8c (0, 0, 0)	16d (1/2, 1/2, 1/2)	16d (1/2, 1/2, 1/2)	16d (1/2, 1/2, 1/2)	16d (1/2, 1/2, 1/2)	16d (1/2, 1/2, 1/2)
OccB/Co [%]	3	25	44	48	49	50	65	62
OccB/Mn [%]	97	75	56	52	51	50	35	38
O	16h (0, y, z) x: 0 y: 0.520 (1) z: 0.2432 (5)	16h (0, y, z) x: 0 y: 0.521(2) z: 0.2436(7)	16h (0, y, z) x: 0 y: 0.5210 z: 0.2423(3)	32e (x, y, z) x: 0.2640 (3) y: 0.2640 (3) z: 0.2640 (3)	32e (x, y, z) x: 0.252(2) y: 0.252(2) z: 0.252(2)	32e (x, y, z) x: 0.2549(0) y: 0.2549(0) z: 0.2549(0)	32e (x, y, z) x: 0.2612(7) y: 0.2612(7) z: 0.2612(7)	32e (x, y, z) x: 0.2614(5) y: 0.2614(5) z: 0.2614(5)
χ^2	1.330	1.35	1.67	1.330	1.35	1.67	1.67	1.29

4.2.2 Morphology through SEM

Scanning electron micrographs depicted in **Figure 4.3(a)**, show the semi-spherical shape for x = 1 and 2, and semi- cuboid shape for x = 1.5. From particle size distribution histogram, average particle size is found to be ~ 96, 74 and 48 nm for x = 1, 1.5 and 2, respectively as shown in **Figure 4.3(b)**. Additionally, the distribution and concentration of Mn and Co are confirmed from the elemental mapping and energy dispersive X-ray spectroscopy (EDS) as shown in **Figure 4.4**. Elemental mapping shows that Mn and Co are homogeneously distributed in nanoparticles and EDS analysis shows the Mn and Co ratio close to 2:1, 1:1 and 1:2, as required in $CoMn_2O_4$, $Co_{1.5}Mn_{1.5}O_4$ and $MnCo_2O_4$, respectively. Thus, it is well corroborated with XRD results and confirms the stoichiometry of $Co_xMn_{3-x}O_4$ nanoparticles.

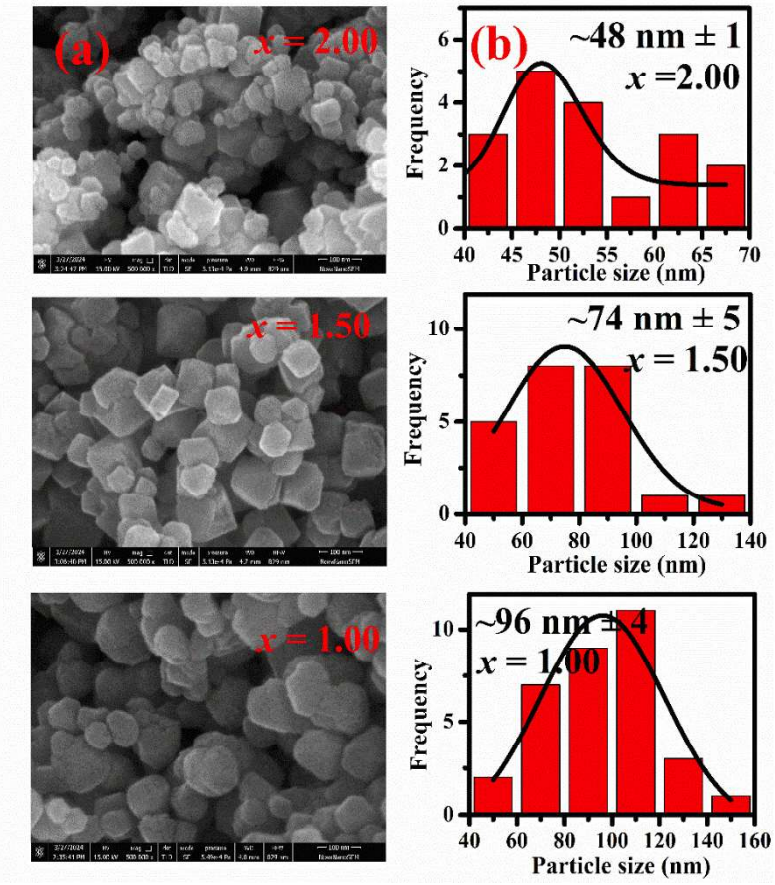

Figure 4.3: SEM images and particle size distribution histogram of $Co_xMn_{3-x}O_4$: (a-b) x = 1.00, (c-d) x = 1.50 and (e-f) x = 2.00.

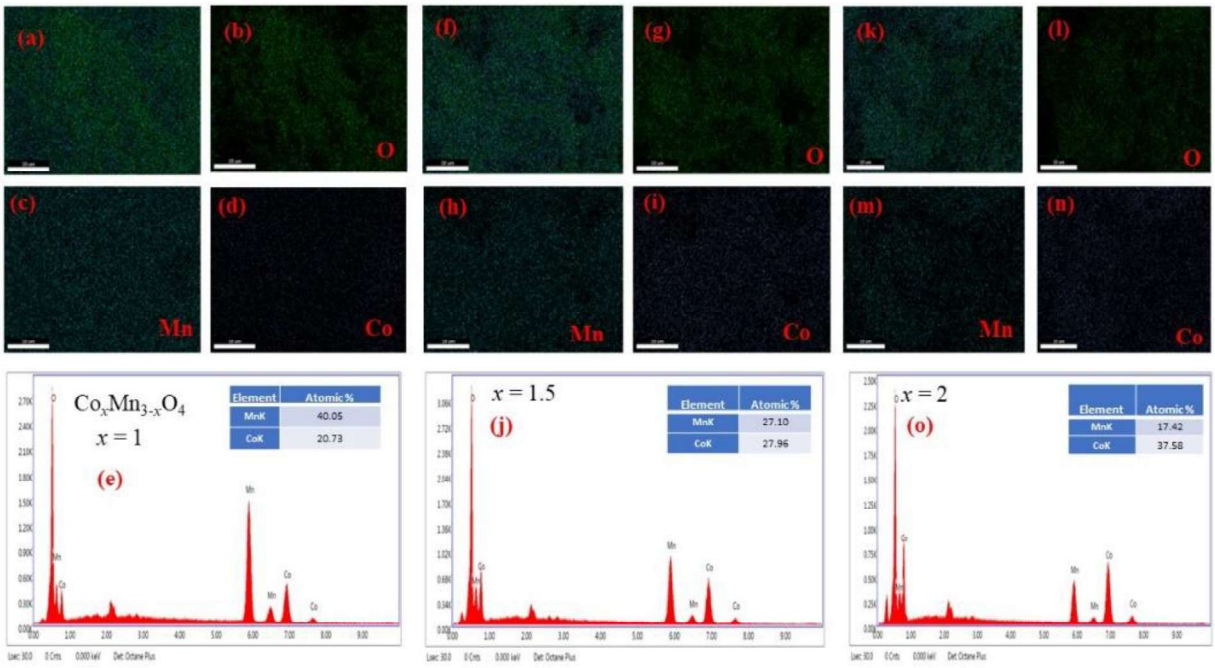

Figure 4.4: Elemental mapping images of $Co_xMn_{3-x}O_4$: (a-d) x = 1.00, (f-i) x = 1.50 and (k-n) x = 2.00, along with energy dispersive spectra, (e) x = 1.00, (j) x = 1.50 and (o) x = 2.00.

4.2.3 XPS for estimation of oxidation state of elements

Further, looking at the distribution of Co and Mn in A and B sites with varying x, the oxidation state by X-ray photoelectron spectroscopy (XPS) is determined for the typical samples with the existence of cubic and tetragonal phase (x = 1.50) and pure cubic phase (x = 2.00). The spectrum is calibrated with carbon-1s peak at 284.6 eV and fitted using XPS peak 4.1 software. **Figure 4.5** shows the XPS spectra for x = 1.50 and 2.00 of Co 2p, Mn 2p and Mn 3s. **Figure 4.5(a and b)** presents the Co 2p spectra of x = 1.50 and 2.00 indicating that there are doublet peaks of Co such as Co $2p_{1/2}$ and Co $2p_{3/2}$ located at 795.4 and 780.2 eV for x = 1.50 and 796.0 and 780.6 eV for x = 2.00, respectively. Apart from these prominent peaks, two satellite peaks at 785.1 and 802.4 eV for x = 1.50 and 785.4 and 802.6 eV for x = 2.00 are obtained. The binding energy separation between Co $2p_{1/2}$ and Co $2p_{3/2}$ is found to be 15.2 and 15.4 eV for x = 1.50 and 2.00, respectively,

indicating the presence of Co^{2+} and Co^{3+} in both samples [83,154]. The asymmetric peaks of Co $2p_{1/2}$ and Co $2p_{3/2}$ are further deconvoluted to find out the percentage of Co^{2+} and Co^{3+}. The estimated concentration of Co^{2+} is found to be 46 and 44%, and 54 and 56% of Co^{3+} for x = 1.50 and 2.00, respectively. Similarly, the spectrum of Mn 2*p* as shown in **Figure 4.5(c and d)**, shows two main peaks for Mn $2p_{1/2}$ and Mn $2p_{3/2}$ at 653.4 and 641.7 eV for x = 1.50 and 652.9 and 641.30 for x = 2.00. Mn 2p spectra have been fitted using four peaks as shown in the figure and the deconvoluted peak confirms the presence of Mn^{2+} for both x = 1.5 and 2.0 [83,154,165]. However, one cannot confirm the presence of Mn^{3+} because Mn^{3+} and Mn^{4+} exhibit significant overlapping [165]. Therefore, we have used Mn 3s spectrum for both samples as shown in **Figure 4.5(e and f).** Here, the strong decrement in the Mn 3s splitting from 5.7 to 4.6 eV is found for x = 1.50 to 2.00, respectively which designates the increment in average oxidation state for x = 2.00. The energy separation of 5.7 eV is associated with the presence of +2 and +3 oxidation states, while the splitting of 4.6 eV denotes the presence of +2 and +4 oxidation states [165–167]. The concentration of Mn^{2+} and Mn^{3+} is about 37 and 63 %, respectively for x =1.50 and 20 % of Mn^{2+} and 80 % of Mn^{4+} for x = 2.00. To confirm the oxidation states found from XPS, XAFS is needed which is discussed in the next section.

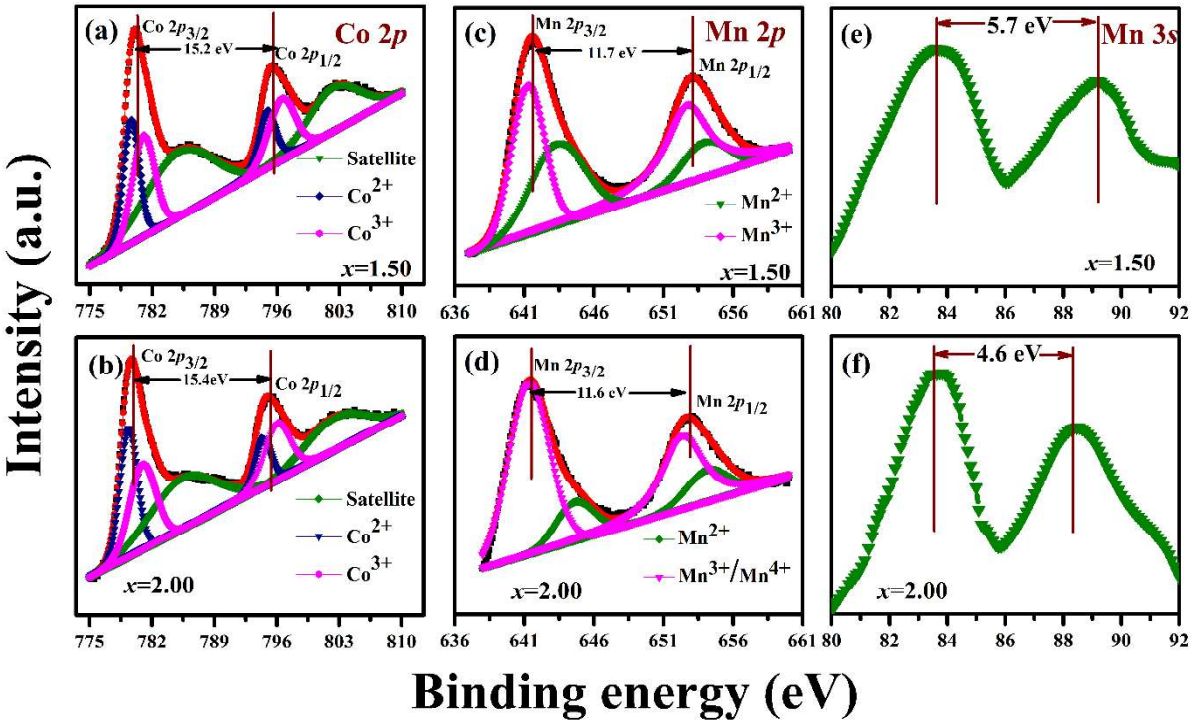

Figure 4.5: X-ray photoelectron spectra of $Co_xMn_{3-x}O_4$ (x = 1.50 and 2.00) nanoparticles, (a and b) Co 2p, (c and d), Mn 2p and (e and f) Mn 3s.

4.2.4 Cation distribution through XAFS analysis

Further to determine the local geometry and fine structure of the sample, XAS analysis is performed. **Figure 4.6(a–d)** depicts the normalized x-ray absorption near edge spectra (XANES) and the pre-edge features recorded at Co and Mn K-edges for $Co_xMn_{3-x}O_4$ (1.00 to 2.00). Previous findings indicate that the pre-edge features primarily arise from electronic transitions between distinct shells where the intensity of the pre-edge peak is notably influenced by the coordination geometry surrounding the absorbing atom [142,168–170]. The intense pre-edge features are mainly detected for the absorbing atom occupying a non-centrosymmetric environment such as tetrahedral site because of the sum of the significantly large electric dipole transition of 1s electron and the p component in 3d–4p hybridised metal orbitals and a small electric quadrupole transition of 1s electron to the 3d orbital [143,168,169]. In a centrosymmetric environment, like a B site, where 3d–4p hybridization is not feasible, the pre-edge peaks are typically less intense. This is

a result of the exclusive occurrence of the electric quadrupole (1s → 3d) transition [142,143,168–170].

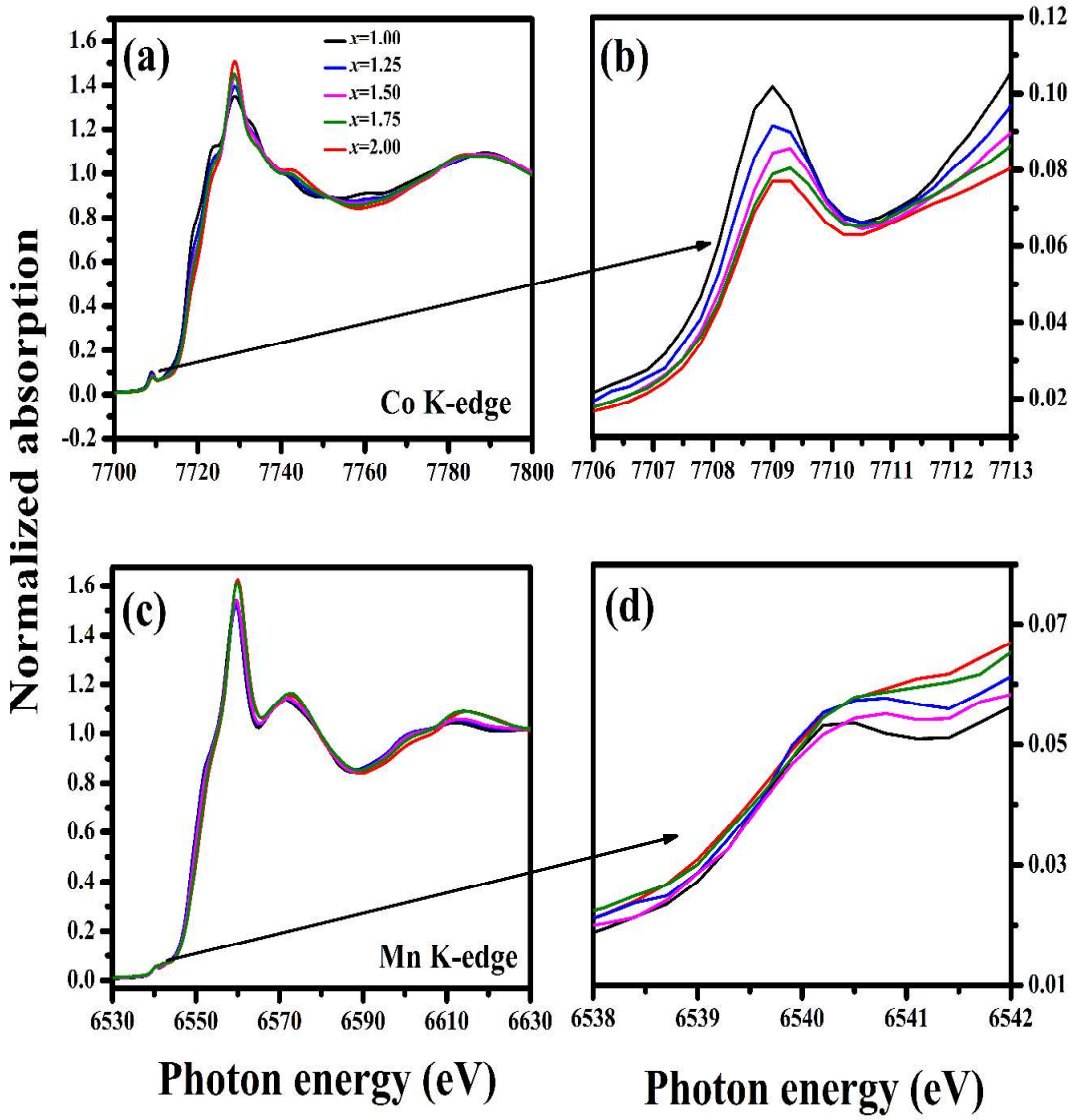

Figure 4.6: XANES spectra collected at the (a) Co K-edge with (b) enlarged view of the corresponding pre-edge region (c) Mn K-edge with (d) enlarged view of the corresponding pre-edge region for $Co_xMn_{3-x}O_4$ (x = 1.00, 1.25, 1.50, 1.75 and 2.00) nanoparticles.

Before the pre-edge feature is analysed, the background of pre-edge peak is subtracted using a spline function that smoothly tracks the data points before and after the pre-edge peak. After that, a Gaussian profile function is used to fit the pre-edge peak of K-edges for transition metals shown in **Figure 4.7** and the results are tabulated in **Tables 4.2-4.3**. The intensity of pre-edge peak is a product of full-width at half maximum (FWHM) and normalised peak height. For Co K-edge, no significant shifting in peaks is found. The most intense pre-edge feature of 0.0765 is obtained at the Co K-edge for x = 1.00, which decreases sharply with an increase in x **(Figure 4.7(a))** and becomes 0.03246 for x = 2.00. Similar feature of pre-edge has been reported by Miyasaka et al. for $CoMn_2O_4$ and Co_3O_4 where the Co ions are considered to be in Co^{2+} and Co^{3+} [114]. In contrast to Miyasaka et al., Bai et al. found two pre-edges for Co in Co_3O_4 where two pre-edges are observed with normal spinel structure [171]. Similar pre-edge feature observed for Co in other spinels indicates the presence of Co^{2+} and Co^{3+} [172–175]. In accordance with the literature, the pre-edge features support the presence of Co^{2+} and Co^{3+} in $CoMn_2O_4$. The decrease in peak intensity with the increase in x is associated with the decrease in cobalt in the tetrahedral site. In case of Mn K-edge, the most intense pre-edge feature obtained for x = 1.00 is found to be decreased with an increase in x as shown in **Figure 4.7(b)**. For x = 1.00, a single pre-edge with centroid at 6540.193 is observed similar to the pre-edge for $CoMn_2O_4$ and Mn_3O_4 [114]. In addition to this, materials like Hausmannite (Mn_3O_4), Braunite (Mn_6SiO_{12}) and Franklinite ($Zn_{0.61}Mn_{0.39}(Fe_{1.94}Mn_{0.06})O_4$) having tetrahedral and octahedral environment with Mn^{2+} and Mn^{3+}, respectively, shows the same pre-edge features for Mn [104,165]. In the present case, the pre-edge intensity (0.0232) is comparatively less than the intensity for non-centrosymmetric site coordinated Mn. Hence, we confirm that Mn occupies mostly the B

site and a decrease in intensity of pre-edge in higher *x* is associated with the decrease of Mn in the B site.

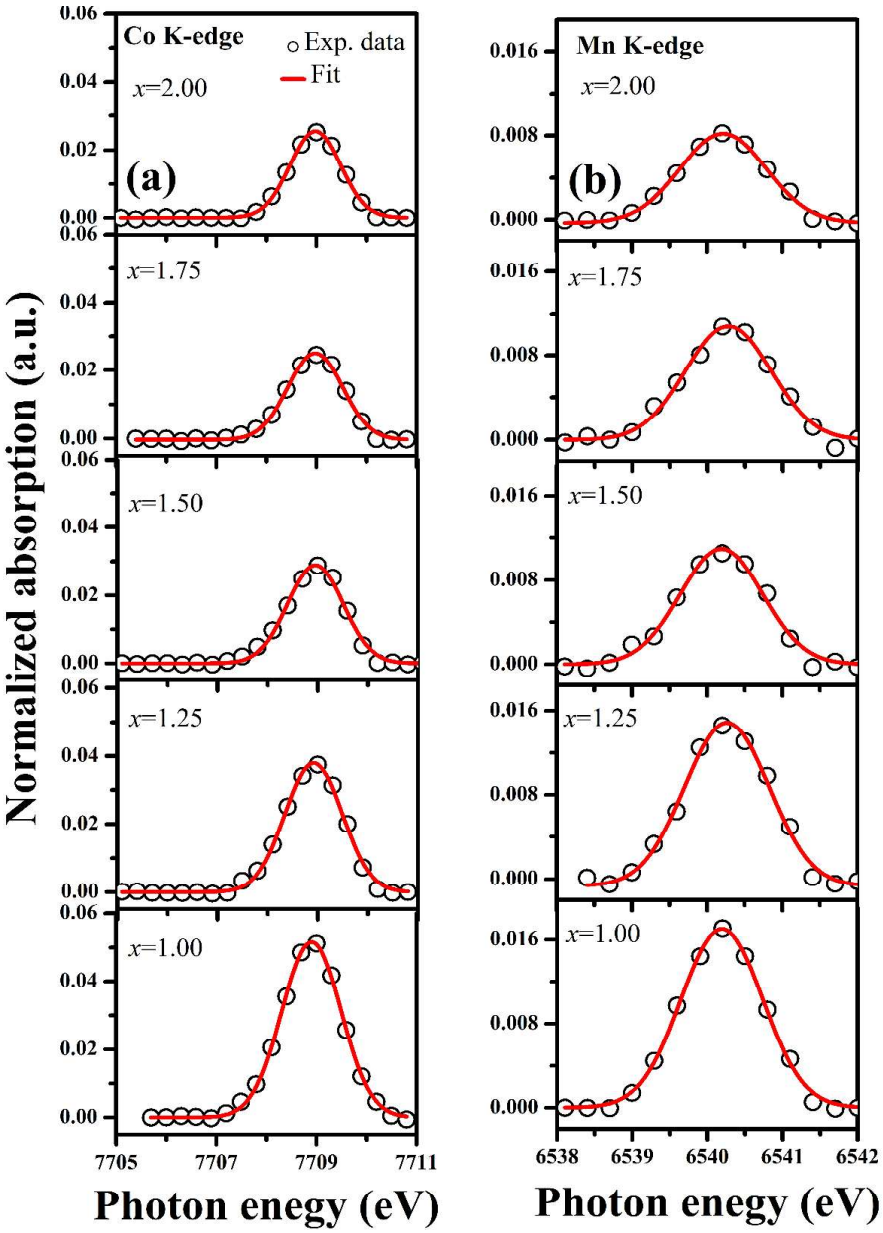

Figure 4.7: Fitting of background subtracted normalized pre-edge peak at Co and Mn K-edges for $Co_xMn_{3-x}O_4$ (x = 1.00, 1.25, 1.50, 1.75 and 2.00) nanoparticles.

Table 4.2: Pre-edge peak information for $Co_xMn_{3-x}O_4$ (x = 1.00, 1.25, 1.50, 1.75 and 2.00) at the Co K-edge.

Sample	Normalized height	Centroid (eV)	FWHM (eV)	Peak intensity	R^2
x =1.00	0.0516(6)	7708.900(4)	1.3935(3)	0.0765(8)	0.9988
x =1.25	0.0379(8)	7708.918(1)	1.3432(0)	0.0542(7)	0.9942
x =1.50	0.0289(2)	7708.953(3)	1.3059(1)	0.0402(0)	0.9906
x =1.75	0.0284(5)	7708.975(1)	1.2858(0)	0.0365(2)	0.9930
x =2.00	0.0254(4)	7708.977(1)	1.1989(9)	0.0324(6)	0.9973

Table 4.3: Pre-edge peak information for $Co_xMn_{3-x}O_4$ (x = 1.00, 1.25, 1.50, 1.75 and 2.00) at the Mn K-edge.

Sample	Normalized height	Centroid (eV)	FWHM (eV)	Peak intensity	R^2
x=1.00	0.0169(8)	6540.193(2)	1.2842(1)	0.0232(0)	0.9960
x=1.25	0.0155(0)	6540.263(8)	1.2544(2)	0.0200(3)	0.9882
x=1.50	0.0109(5)	6540.191(5)	1.3009(2)	0.0151(5)	0.9810
x=1.75	0.0107(7)	6540.277(9)	1.3427(8)	0.0154(0)	0.9844
x=2.00	0.0084(8)	6540.213(5)	1.3650(1)	0.0123(1)	0.9844

Figure 4.8(a and b) shows the Fourier transform (FT) EXAFS spectra at Co and Mn K-edges without phase corrections. In the Co K-edge spectrum, three prominent peaks emerge at distances 1.6 Å, 2.4 Å, and 3.0 Å for x = 1.00 **(Figure 4.8(a)**. First peak is attributed to the interaction of absorber Co with its first nearest neighbour oxygen, whereas second and third peak correspond to the scattering from the cations at the B and A sites, respectively. The maximum intensity of the peak at 3 Å suggests a predominant

presence of Co ions in the A site in $CoMn_2O_4$ [114]. Furthermore, an increase in the intensity of the peak at 2.4 Å, suggests an increase of cobalt at B site. For Mn K-edge spectra, two dominant peaks and a small peak are observed for pure cubic samples i.e. x = 1.75 and 2.00, where the first peak at 1.52 Å is associated with the first nearest neighbour i.e., oxygen (Mn-O). While the peak at 2.5 Å corresponds to the scattering from the B site cations, the small peak at 3.21 Å corresponds to the scattering from A site [114,176,177]. As we decrease x from 2.00 to 1.00, there is no significant change in the peak at 1.52 Å. However, the second peak corresponding to 2.5 Å starts splitting into two peaks at ~2.4 and 2.78 Å for x = 1.00, 1.25 and 1.50, where tetragonal and cubic phases coexist **(Figure 4.8(b)**. Here, the splitting of the peak could be ascribed to the two different atomic distances due to Jahn-Teller distortion for tetragonal phase. However, for x = 1.00, the intensity of former peak is higher compared to the latter one could be due to the presence of cubic phase in addition to tetragonal phase [114]. Thus, the qualitative analysis of EXAFS is well corroborated with the XRD results. The exact information of local structure is found from EXAFS fitting by using the Demeter package (Athena, Artemis, and Hephaestus) [146]. The FT-EXAFS spectra are fitted at K-edge of each transition metal over a range of 1–4 Å.

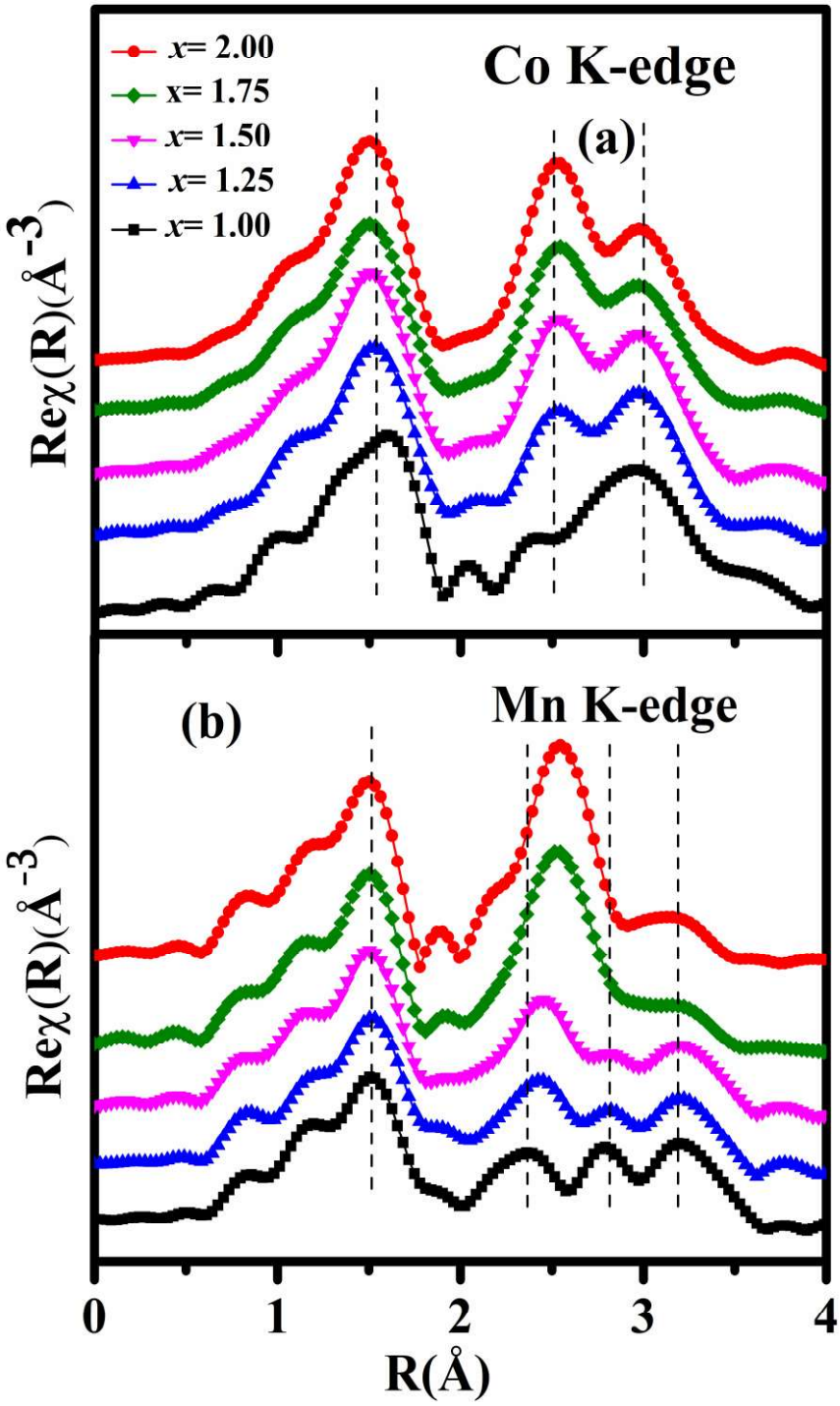

Figure 4.8: Fourier transforms magnitude of EXAFS spectra of (a) Co K-edge (b) Mn K-edge for $Co_xMn_{3-x}O_4$ (x = 1.00, 1.25, 1.50, 1.75 and 2.00) nanoparticles.

We have considered the structural information like lattice parameters and atomic coordinates found from the Rietveld refinement as the input to produce the FEFF file. To fit the coexistence of tetragonal and cubic phase (x = 1.0, 1.25, 1.50), we have considered

Co and Mn to be present at both A and B sites in both the phases and hereafter they are denoted as Co_A, Co_B, Mn_A, and Mn_B. In this case, four theoretical models are needed to fit the EXAFS spectra. However, due to the limitation of parameters, fitting of the spectra becomes very complicated. Besides, Rietveld refinement has shown approximately equal bond length for A-B corresponding to both the phases. Therefore, for samples having both cubic and tetragonal phases we have assumed the following points. In tetragonal phase, Mn occupies the B site and Co occupies the A site while in cubic phase Mn occupies the A site and Co occupies the B site. Hence the fractional distribution α, here signifies the contribution of phase present in the sample. Therefore, at Co K-edge, theoretical models are used to fit the FT-EXAFS spectra in tetragonal phase where Co absorber atom is considered to occupy A site with Mn_B scatterer and in cubic phase Co absorber occupies B site with Mn_A scatterer. At Mn K-edge, Mn absorber is considered to occupy B site with Co_A scatterer in tetragonal phase and cubic phase Mn absorber occupy A site with Co_B scatterer. In pure cubic phase (x = 1.75 and 2.0), Co and Mn are considered to be present at both A and B sites. Therefore, the fractional distribution α, signifies the presence of ions at the particular site i.e., the amount of Co/Mn present at the A and B site in cubic phase. Here, two theoretical models are used in both Co and Mn absorber atom. At the Co K-edge, first theoretical model is used to fit the FT-EXAFS spectra where Co is considered in the A site (Co_A) with the Mn_B scatterer, while in second model, Co absorber is considered in B site (Co_B) with Mn_A as scatterer. For Mn K-edge, Mn absorber atom is considered in the A site (Mn_A) with the Co_B as scatterer in the former model, while in latter model Mn absorber atom is considered in the B site (Mn_B) with the Co_A as the scatterer. The FT-EXAFS spectra are fitted without using any photoelectron scattering phase-shift correction for $Co_xMn_{3-x}O_4$ (x = 1.00, 1.25, 1.50, 1.75 and 2.00). The element specific amplitude reduction factor (S_0^2) depends on α and the amplitude. α is

varied at the time of fitting and amplitude is determined from the reference sample. Therefore, it is constant for all the samples and is estimated to be ~ 0.823 for Co and ~ 0.986 for Mn. The S_0^2 parameter varies with α at the time of fitting at Co and Mn K-edges. Throughout the refinement process, the energy correction (E_0) parameter is varied and constrained for every path. Debye–Waller factor (σ^2) and bond-length (R) are varied during the fitting. To reduce the number of fitting variables, σ^2 is the same for some single scattering paths of Mn-O and Co-O corresponding to the first coordination shell of both A and B sites. No constraint is applied for the parameter R obtained from Co and Mn absorber/scatterer. **Figure 4.9 and 4.10** show the fitting of the EXAFS spectra of Co and Mn, respectively, in the k-space ($Å^{-1}$) magnitude and real part in the R-space (Å). It should be mentioned that the FT-EXAFS spectra are fitted using only the single scattering path because the use of multiple scattering paths increases the residual factor (R-factor) and χ^2 with the large statistical relationship between the fitted parameters. The best EXAFS fitting parameters are tabulated in **Tables 4.4-4.7**. Fitting parameters for Co K-edge shown in **Tables 4.4 and 4.5** demonstrate that increasing Co concentration does not lead to significant changes in the Debye–Waller (σ^2) factor and bond length. The Co_A–O average bond length of 1.960–1.978 Å obtained from the fitting is consistent with the Co–O average bond length of 1.96-1.98 Å reported in literatures for A site occupied Co^{2+} [178]. Similarly, Co_B-O bond length for x = 1.00 to 1.50 is found to be 2.075-2.00 Å supports the B site occupancy of Co as reported in the literature **(Table 4.4)** [178]. However, with an increase in x to 1.75 and 2.0, Co_B-O average bond length decreases to ~1.96 Å which indicates the presence of some higher valency of Co in the B site as shown in **Table 4.5.** For Mn K-edge, there is no significant change found in Mn_A-O average bond length when x increases from 1.0 to 2.0 shown in **Tables 4.6 and 4.7**. Mn_A-O bond length is found in the range of 2.15-2.19 Å supports the presence of Mn^{2+} in A site as per the literature [178].

Mn_B-O average bond length is found to be decreased compared to Mn_A-O when x increases from 1.00 to 1.50. Mn_B-O average bond length of ~ 2.214-2.01 Å supports the Mn^{3+} occupancy in B site (**Table 4.6**) [178]. Furthermore, a significant decrement in Mn_B-O average bond length is noticed when x increases to 1.75 and above. The bond length is found to be ~1.926 Å which specifies the presence of Mn^{4+} in B site (**Table 4.7**). This shows that in A site bond length does not change when x increases from 1.00 to 2.00 and the decrement in the average bond length in B site with increase in x to 1.75 and 2.00 designates the increase in average oxidation state of Mn in B site.

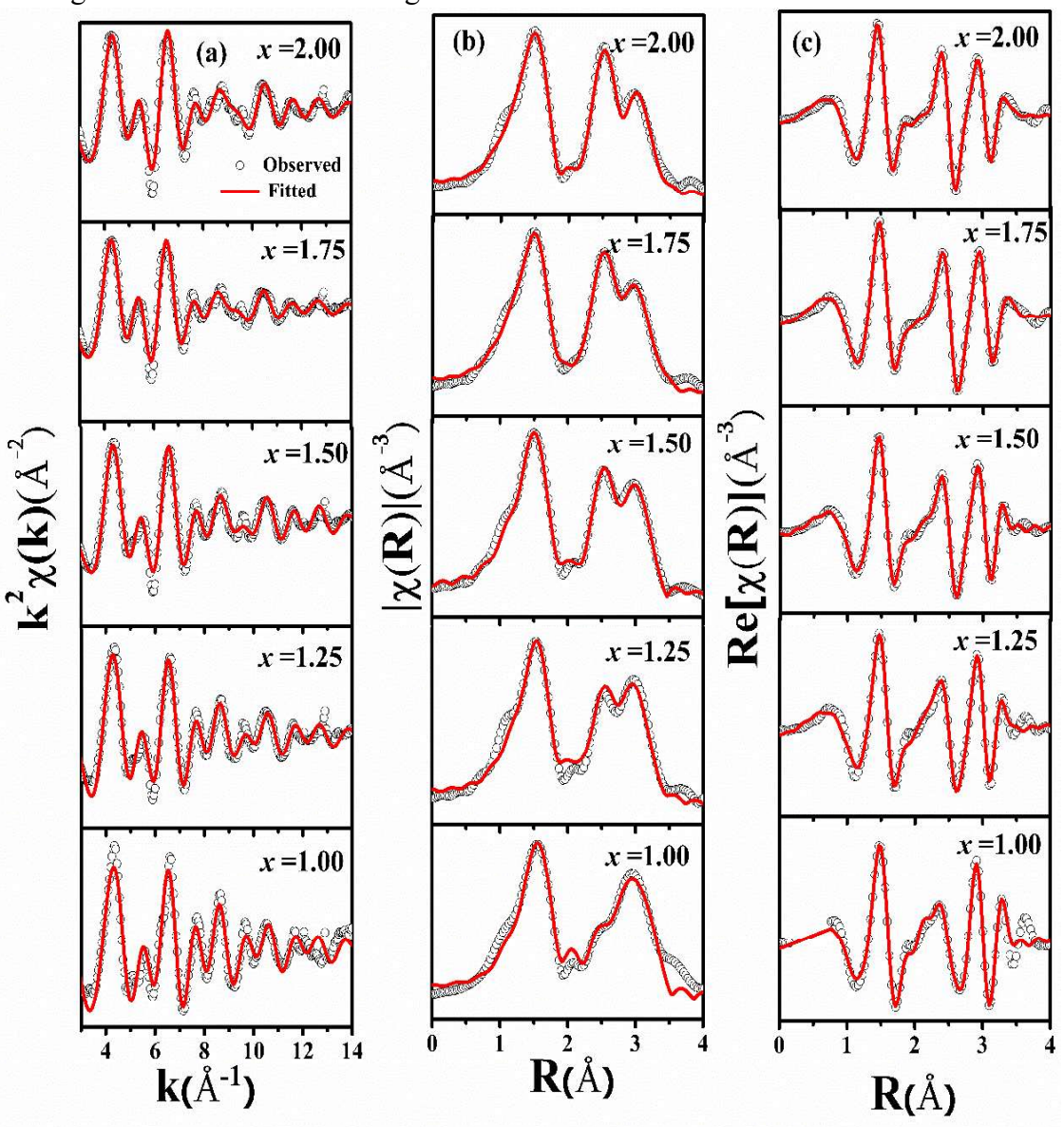

Figure 4.9: EXAFS spectra fitted with the theoretical pattern in (a) k-space ($Å^{-1}$) (b) magnitude part of R-space (Å) and (c) real part of R-space (Å) with k^2-weighting at the Co K-edge for $Co_xMn_{3-x}O_4$ (x = 1.00, 1.25, 1.50, 1.75 and 2.00) nanoparticles.

Table 4.4: Fitting results of the FT EXAFS spectra at the Co K-edge for the samples having coexistence of cubic and tetragonal phase i.e., for $Co_xMn_{3-x}O_4$ (x = 1.00, 1.25 and 1.50).

Path	Parameter	x = 1.00	x = 1.25	x = 1.50
[Co_A-O]T N (4)	ΔE_0 (eV) R (Å) σ^2 (Å^2) amp α	4.0(6) 1.96(1) 0.003(2) 0.823 0.878(0)	2.1(1) 1.97(4) 0.004(1) 0.823 0.80(7)	0.8(9) 1.97(1) 0.004 (1) 0.823 0.64(5)
[Co_B-O]C N (6)	ΔE_0 (eV) R (Å) σ^2 (Å^2)	4.0(6) 2.075(0) 0.0030(0)	2.1(2) 2.001(1) 0.0040(9)	0.8(9) 2.00 (0) 0.005(5)
[Co_A- Mn_B]T N (8)	ΔE_0 (eV) R (Å) σ^2 (Å^2)	4.0(6) 3.41(0) 0.006(0)	2.1(1) 3.39(4) 0.007(1)	0.8(9) 3.40(1) 0.005(1)
[Co_B-Co_A]C N (6)	ΔE_0 (eV) R (Å) σ^2 (Å^2)	4.0(6) 2.912(0) 0.007(0)	2.1(2) 2.88(2) 0.000(1)	0.8(9) 2.88(7) 0.005(5)

Table 4.5: Fitting results of the FT EXAFS spectra at the Co K-edge for the samples having cubic phase i.e., for x = 1.75 and 2.00.

Path	Parameter	x = 1.75	x = 2.00
[Co_A-O] N (4)	ΔE_0 (eV) R (Å) σ^2 (Å^2) amp α	1.4(5) 1.969 (0) 0.004(1) 0.823 0.552(0)	0.8 (6) 1.978(0) 0.000 (1) 0.823 0.49 (6)
[Co_B-O] N (6)	ΔE_0 (eV) R (Å) σ^2 (Å^2)	1.4(5) 1.961(6) 0.006(0)	0.8 (6) 1.96(1) 0.000 (1)
[Co_B-Co_A] N (6)	ΔE_0 (eV) R (Å) σ^2 (Å^2)	1.4(5) 2.890(5) 0.007(0)	0.8 (6) 2.871 (5) 0.005 (1)
[Co_B-Mn_A] N (6)	ΔE_0 (eV) R (Å) σ^2 (Å^2)	1.4(5) 3.51(1) 0.004 (1)	0.8 (6) 2.871 (5) 0.005 (1)
[Co_A-Mn_B] N (12)	ΔE_0 (eV) R (Å) σ^2 (Å^2)	1.4(5) 3.390 (9) 0.005(1)	0.8 (6) 3.408 (5) 0.009 (1)

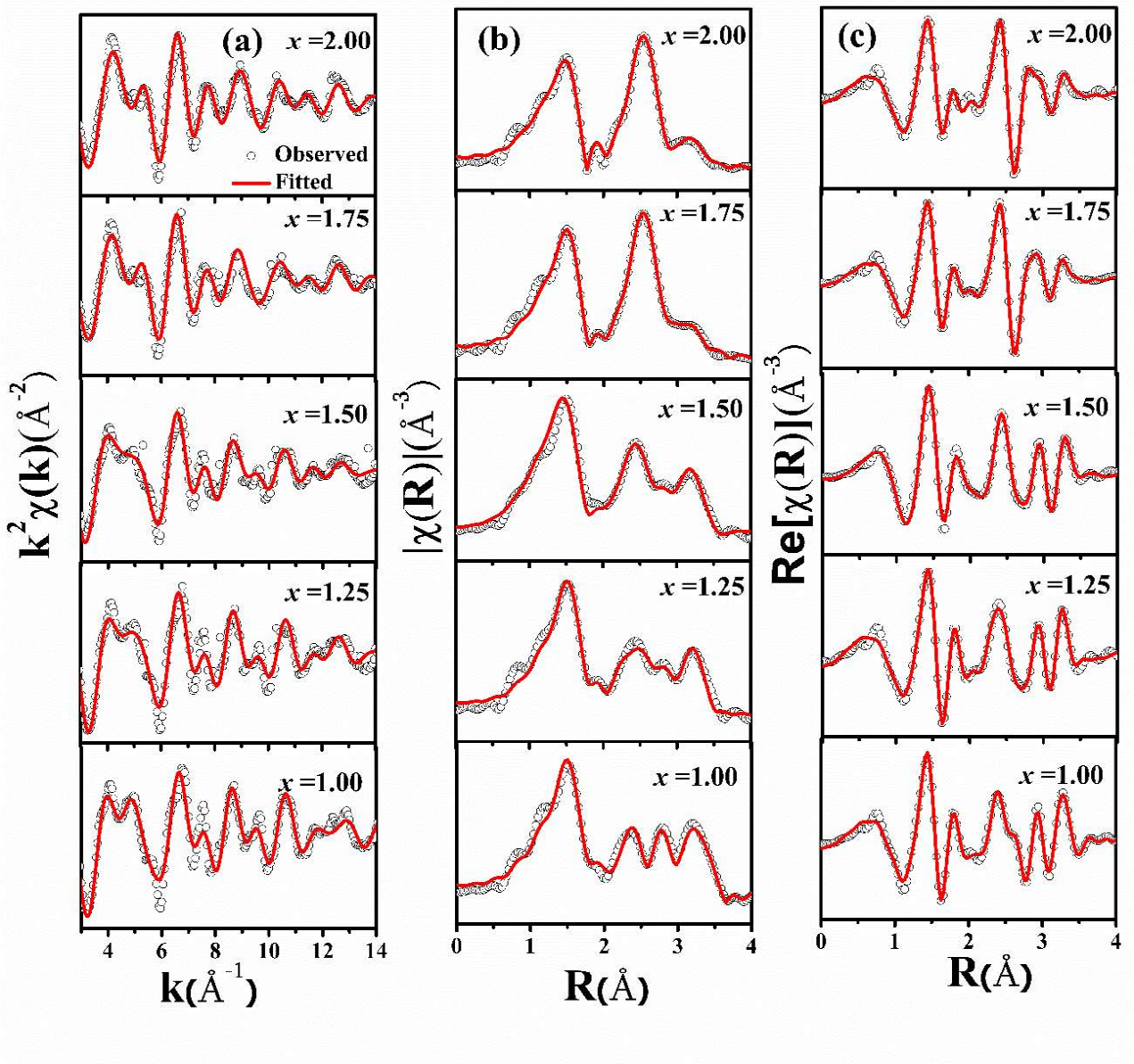

Figure 4.10: EXAFS spectra fitted with the theoretical pattern in (a) k-space ($Å^{-1}$) (b) magnitude part of R-space (Å) and (c) real part of R-space (Å) with k^2-weighting at the Mn K-edge for $Co_xMn_{3-x}O_4$ (x = 1.00, 1.25, 1.50, 1.75 and 2.00) nanoparticles

Table 4.6: Fitting results of the FT EXAFS spectra at the Mn K-edge for the samples having coexistence of cubic and tetragonal phase i.e., for $Co_xMn_{3-x}O_4$ (x = 1.00,1.25, and 1.50).

Path	Parameter	x = 1.00	x = 1.25	x = 1.50
$[Mn_A$ - O]C N (4)	ΔE_0 (eV) R (Å) σ^2 (Å^2) amp α	2.2(4) 2.15(3) 0.003(0) 0.986 0.87(8)	3.6(6) 2.25(1) 0.002(4) 0.986 0.70(1)	-3.9(9) 2.164(0) 0.005(1) 0.986 0.56(8)
$[Mn_B - O_{eq}]$T N (4)	ΔE_0 (eV) R (Å) σ^2 (Å^2)	2.2(4) 1.93(1) 0.003 (0)	3.6(6) 1.924(4) 0.002(4)	-3.9(9) 1.894(0) 0.005(1)
$[Mn_B$- $O_{ax}]$T N (2)	ΔE_0 (eV) R (Å) σ^2 (Å^2)	2.2(4) 2.27(1) 0.006(1)	3.6(6) 2.15(3) 0.016 (3)	-3.9(9) 2.262(0) 0.005(1)
$[Mn_B$- $O_{ave}]$T	R (Å)	2.214	2.00	2.010
$[Mn_B$ - $Mn_A]$T N (2)	ΔE_0 (eV) R (Å) σ^2 (Å^2)	2.2(4) 2.874(8) 0.003(1)	3.6(6) 2.47(2) 0.016(3)	-3.9(9) 3.07(8) 0.007(1)
$[Mn_B$ - $Mn_A]$T N (4)	ΔE_0 (eV) R (Å) σ^2 (Å^2)	2.2(4) 3.067(8) 0.006(1)	3.6(6) 2.97(2) 0.013(1)	-3.9(9) 2.90(2) 0.007(1)
$[Mn_B$ - $Co_A]$T N (4)	ΔE_0 (eV) R (Å) σ^2 (Å^2)	2.2(4) 3.802(0) 0.017(7)	3.6(6) 3.145(0) 0.006(2)	-3.9(9) 3.33(5) 0.007(1)
$[Mn_A$ - $Co_B]$C N (12)	ΔE_0 (eV) R (Å) σ^2 (Å^2)	2.2(4) 3.546(0) 0.017(7)	3.6(6) 3.399(4) 0.006(2)	-3.9(9) 3.43 (5) 0.007(1)
$[Mn_A$ - $Mn_B]$C N (4)	ΔE_0 (eV) R (Å) σ^2 (Å^2)	2.2(4) 3.423(0) 0.000(0)	3.6(6) 3.435(0) 0.046 (0)	-3.9(9) 3.73(3) 0.006 (1)

Table 4.7: Fitting results of the FT EXAFS spectra at the Mn K-edge for the samples having cubic phase i.e., for $Co_xMn_{3-x}O_4$ (x = 1.75, and 2.00).

Path	Parameter	x = 1.75	x = 2.00
[Mn_A – O] N (4)	ΔE_0 (eV)	0.5(7)	1.9 (9)
	R (Å)	2.24(2)	2.19 (5)
	σ^2 (Å^2)	0.009(4)	0.005(1)
	amp	0.986	0.986
	α	0.625(4)	0.69(5)
[Mn_B - O] N (6)	ΔE_0 (eV)	0.5(7)	1.9 (9)
	R (Å)	1.926(5)	1.926(7)
	σ^2 (Å^2)	0.004(1)	0.005(1)
[Mn_B - Mn_A] N (6)	ΔE_0 (eV)	0.5(7)	1.9 (9)
	R (Å)	2.932(5)	2.932(6)
	σ^2 (Å^2)	0.005(0)	0.005 (0)
[Mn_B – Co_A] N (6)	ΔE_0 (eV)	0.5(7)	1.9 (9)
	R (Å)	3.40(1)	3.43(2)
	σ^2 (Å^2)	0.007 (1)	0.010(2)

4.3 Conclusion

The structure, local structure and microstructure of $Co_xMn_{3-x}O_4$, where x = 1.00, 1.25, 1.50, 1.75 and 2.00 synthesized via coprecipitation technique were studied. X-ray diffraction spectrum fitted with Rietveld refinement showed the coexistence of tetragonal and cubic phases upto x = 1.50, above which pure cubic phase existed. Further, XPS indicated the presence of both +2 and +3 valency for both Co and Mn, whereas for pure cubic phase, Mn was present in the higher oxidation state (+4). In addition, the EXAFS spectra were fitted with two phases for the first time which provided a new insight for understanding the local structure of $Co_xMn_{3-x}O_4$ spinels. The cation distribution obtained from X-ray absorption fine structure analysis illustrated that Mn^{3+} and Co^{2+} ions mainly occupied B and A sites, respectively for x = 1.00. With the increase in x, Co^{3+} started replacing Mn^{3+} ions. When x increased to 1.75 a significant decrement in average bond length of Mn_B-O in EXAFS fitting specified the presence Mn^{4+} ions which supported the XPS results.